

4D Gaussian Splatting with Scale-aware Residual Field and Adaptive Optimization for Real-time Rendering of Temporally Complex Dynamic Scenes

Jinbo Yan

yjb@stu.pku.edu.cn

School of Electronic and Computer Engineering, Peking University
Shenzhen, China

Luyang Tang

tly926@stu.pku.edu.cn

School of Electronic and Computer Engineering, Peking University
Shenzhen, China

Rui Peng

ruipeng@stu.pku.edu.cn

School of Electronic and Computer Engineering, Peking University
Shenzhen, China

Ronggang Wang*

rgwang@pkusz.edu.cn

School of Electronic and Computer Engineering, Peking University
Shenzhen, China
Pengcheng Laboratory
Shenzhen, China

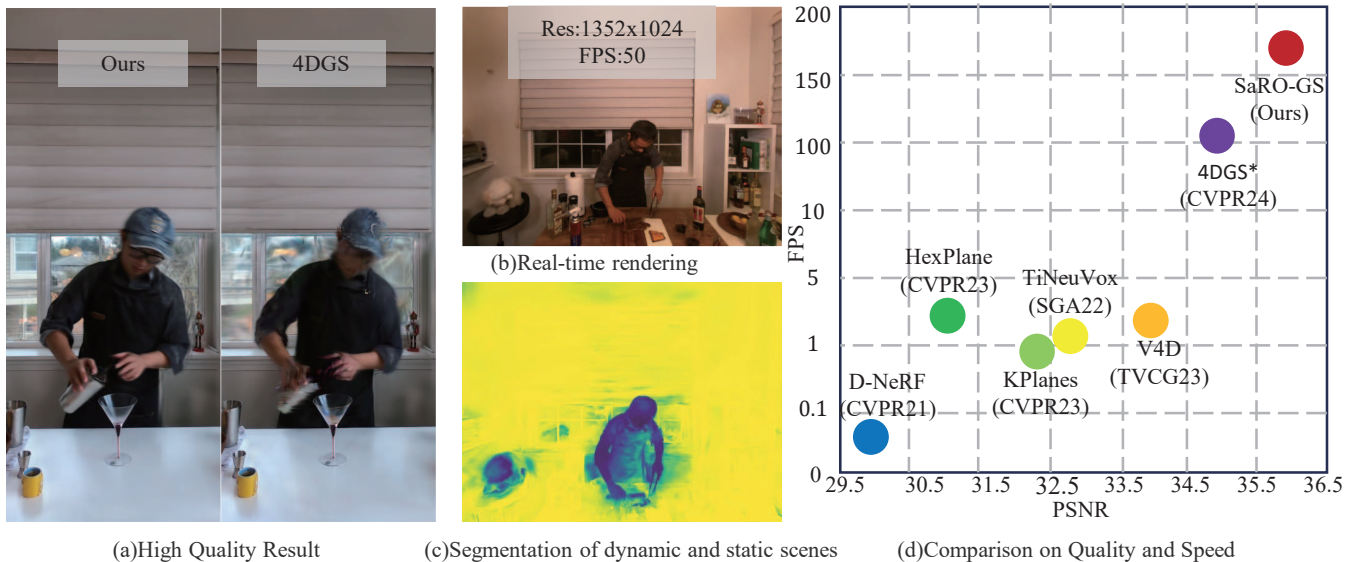


Figure 1: Performance comparison with previous SOTA[7, 12, 13, 15, 42, 61]. Our approach achieves higher-quality reconstruction in temporally complex scenes (a) while maintaining real-time rendering (b), with a certain improvement in performance(c). Additionally, we achieve dynamic scene segmentation without any prior information (c).*:measured by us at 400x400 resolution.

*Corresponding author.

Permission to make digital or hard copies of all or part of this work for personal or classroom use is granted without fee provided that copies are not made or distributed for profit or commercial advantage and that copies bear this notice and the full citation on the first page. Copyrights for components of this work owned by others than the author(s) must be honored. Abstracting with credit is permitted. To copy otherwise, or republish, to post on servers or to redistribute to lists, requires prior specific permission and/or a fee. Request permissions from permissions@acm.org.

MM '24, October 28–November 1, 2024, Melbourne, VIC, Australia

© 2024 Copyright held by the owner/author(s). Publication rights licensed to ACM.

ACM ISBN 979-8-4007-0686-8/24/10

<https://doi.org/10.1145/3664647.3681463>

Abstract

Reconstructing dynamic scenes from video sequences is a highly promising task in the multimedia domain. While previous methods have made progress, they often struggle with slow rendering and managing temporal complexities such as significant motion and object appearance/disappearance. In this paper, we propose SaRO-GS as a novel dynamic scene representation capable of achieving real-time rendering while effectively handling temporal complexities in dynamic scenes. To address the issue of slow rendering speed, we adopt a Gaussian primitive-based representation and optimize the Gaussians in 4D space, which facilitates real-time rendering with

the assistance of 3D Gaussian Splatting. Additionally, to handle temporally complex dynamic scenes, we introduce a Scale-aware Residual Field. This field considers the size information of each Gaussian primitive while encoding its residual feature and aligns with the self-splitting behavior of Gaussian primitives. Furthermore, we propose an Adaptive Optimization Schedule, which assigns different optimization strategies to Gaussian primitives based on their distinct temporal properties, thereby expediting the reconstruction of dynamic regions. Through evaluations on monocular and multi-view datasets, our method has demonstrated state-of-the-art performance. Please see our project page at <https://yjb6.github.io/SaRO-GS.github.io/>.

CCS Concepts

• **Computing methodologies** → **Rendering**.

Keywords

Real-time rendering, Dynamic scene reconstruction

ACM Reference Format:

Jinbo Yan, Rui Peng, Luyang Tang, and Ronggang Wang. 2024. 4D Gaussian Splatting with Scale-aware Residual Field and Adaptive Optimization for Real-time Rendering of Temporally Complex Dynamic Scenes. In *Proceedings of the 32nd ACM International Conference on Multimedia (MM '24)*, October 28–November 1, 2024, Melbourne, VIC, Australia. ACM, New York, NY, USA, 14 pages. <https://doi.org/10.1145/3664647.3681463>

1 INTRODUCTION

The reconstruction of dynamic scenes is pivotal for immersive imaging, driving advancements in various multimedia technologies such as VR, AR, and metaverse. Our objective is to reconstruct a continuous 4D space from a discrete temporal video sequence. However, this endeavor faces several challenges. Firstly, the reconstruction quality acts as a bottleneck for widespread adoption, requiring accurate capture of spatial dimensions and temporal variations in dynamic scenes. Additionally, there's a growing demand for real-time interaction in multimedia products to boost user engagement, highlighting the importance of achieving real-time rendering. Nevertheless, existing methods struggle to achieve both high-quality reconstruction and real-time rendering simultaneously, precisely the issue our approach aims to tackle.

Recent advancements in dynamic scene reconstruction have been achieved through methods based on NeRF [32] and 3DGS [22]. NeRF employs an implicit field to model static scenes and achieves photo-realistic view synthesis. Many extensions of NeRF to dynamic scenes either utilize deformation fields and canonical fields to model the motion of objects relative to canonical frames over time [18, 29, 36, 42, 51, 53], or decompose the 4D volume into spatial-only and spatial-temporal spaces [7, 13, 28, 49], representing space through combinations of dimensionally reduced features. While significant progress has been made in rendering quality, these methods face a significant disadvantage in rendering speed. The emergence of 3DGS has enabled real-time rendering of dynamic scenes. Some methods [21, 27, 61, 64, 65] have attempted dynamic scene modeling based on 3DGS. However, they either struggle to model temporally complex scenes such as object appearances and disappearances [21, 61, 64] or overlook the spatiotemporal

information in the scene [27, 65], resulting in disadvantages when dealing with temporally complex dynamic scenes.

To address the aforementioned challenges, we propose SaRO-GS, aiming to achieve real-time rendering while maintaining high-quality reconstruction of temporally complex dynamic scenes. SaRO-GS comprises a set of Gaussian primitives in 4D space and a Scale-aware Residual Field. Each Gaussian receives a unique optimization schedule based on its distinct temporal properties through an Adaptive Optimization strategy. To address the issue of slow rendering speeds, Gaussian primitives in 4D space can be projected to 3D based on their temporal properties and residual features obtained from the Scale-aware Residual Field. Then we can achieve real-time rendering leveraging the fast differentiable rasterizer introduced by 3DGS. For high-quality modeling of temporally complex scenes, we employ the following strategies: Firstly, each 4D Gaussian primitive possesses temporal properties, including temporal position and lifespan. The lifespan allows us to model the appearance and disappearance of objects in dynamic scenes, while the temporal position of Gaussians spans the entire temporal range, rather than being fixed at frame 0 as in previous methods. Additionally, we incorporate scale information of Gaussian primitives into the Residual Field to accommodate their ellipsoidal nature. By encoding the region that the Gaussian primitives occupy rather than just their position, we ensure accurate feature extraction and align with the self-splitting behavior of Gaussian primitives. Thirdly, we introduce an Adaptive Optimization strategy, where unique optimization strategies are assigned to each Gaussian primitive based on its temporal properties, facilitating faster reconstruction of dynamic regions.

We extensively evaluated our approach on monocular and multi-view dynamic scene datasets, comprising both real and synthetic scenes. Both quantitative and qualitative results demonstrate that our method achieves high-quality rendering in real time and effectively handles temporal complexities in dynamic scenes. Our contributions are summarized below.

- We propose a Scale-aware Residual Field, incorporating the scale information of Gaussians. This results in a more precise spatiotemporal representation, considering Gaussian primitives' ellipsoidal nature and self-splitting behavior.
- We introduce an Adaptive Optimization strategy, assigning unique optimization schedule to Gaussians based on their unique temporal properties, enhancing the reconstruction of dynamic areas.
- Our SaRO-GS excels in managing temporally complex scenarios, delivering state-of-the-art performance in both the reconstruction quality and rendering speed. It achieves an 80x rendering speed improvement compared to NeRF-based methods as shown in Fig. 1. SaRO-GS is versatile, applicable to both monocular and multi-view scenarios and can also achieve dynamic scene segmentation without any prior.

2 RELATED WORK

2.1 Static Scene Representation

Significant progress has been made in various fields related to the task of static scene representation, including image matching [30, 45, 50], camera calibration [46, 47], depth estimation [11, 16, 17, 39], and

Multi-View Stereo[39, 62, 66, 67, 75–77], among others. Recently, there has been a growing interest in the use of Neural Radiance Fields as a means of representing static scenes. NeRF[32], as a representative work, models static scenes as a radiance field and synthesizing images through volume rendering. The photo-realistic view synthesis capability of NeRF has inspired a series of works across various domains, including enhancing rendering quality[4–6, 8, 54, 55, 72, 74], sparse inputs[3, 34, 63], surface representation and segmentation[38, 59, 79], accelerating training and rendering[6, 14, 19, 20, 33, 43, 44, 49, 52, 69, 73], as well as human modeling[40, 41, 60, 71, 80], among others. Recently, there has been a breakthrough in high-quality view synthesis and real-time rendering with 3D Gaussian Splatting[22] and relate works[24, 70, 78, 81], garnering significant attention in the scene reconstruction field.

2.2 Dynamic Scene Representation

Expanding static scene representation to dynamic scenes is not a simple task. Some NeRF based methods[18, 29, 36, 42, 51, 53] have made progress based on deformation fields, modeling the entire scene as a canonical field and a deformation field. They use the deformation field to represent the association between sampled points under different frames and the static canonical. Other methods[7, 13, 28, 49, 56] reduce the dimensionality of the 4D space by decomposing it into a set of planar grids or hash grids. This approach effectively models temporal correlations through spatiotemporal grids. Furthermore, some methods[25, 58] adopt a streaming strategy to model residuals between adjacent frames, which is suitable for real-time transmission and decoding. However, these rendering approaches based on NeRF requires dense sampling along rays during rendering, limiting the possibility of real-time rendering.

There are some concurrent works based on 3D Gaussian for dynamic scenes. [31] uses an online strategy to model dynamic scenes frame by frame, [61] uses a Hex-planes to model the changes of Gaussian primitives over sampling time. Both of them struggle to handle temporal complexities, such as significant motion and object appearances/disappearances. [65] introduces a time dimension to Gaussian, enabling 4D Gaussian to be decomposed into a conditional 3D Gaussian and a marginal 1D Gaussian. In comparison, we propose an Scale-aware Residual field to model the residual of Gaussian primitives projected from 4D to 3D, employing an explicit-implicit blending approach that better incorporates spatiotemporal correlations. Other methods like [27] are not suitable for monocular scenarios, and [64] cannot be utilized in multi-view scenes. In contrast, our approach, validated through experiments, demonstrates promising results in both single-view and multi-view scenarios.

3 PRELIMINARY

3.1 3D Gaussian Splatting

Given a set of input images of a static scene along with their corresponding camera parameters, 3D Gaussian Splatting (3DGS) initiates the reconstruction of the static scene from an initial point cloud, employing 3D Gaussians as primitives. This approach enables high-quality real-time novel view synthesis.

In 3DGS, each Gaussian primitive encompasses a set of attributes, including 3D position μ_{3d} , opacity α , and covariance matrix Σ . A

3D Gaussian \mathcal{G} can be represented as:

$$G(x) = e^{-\frac{1}{2}(x-\mu)^T \Sigma^{-1}(x-\mu)} \quad (1)$$

For optimization convenience, 3DGS employs a scaling matrix S and a rotation matrix R to represent covariance, stored as a 3D vector s for scaling and a quaternion q for rotation.

$$\Sigma = RSS^T R^T \quad (2)$$

Additionally, 3DGS utilizes SH coefficients to represent view-dependent color.

Based on the fast differentiable rasterizer implemented by 3DGS, we can achieve rapid image rendering through Gaussian Splatting. To get the rendering images from a given viewpoint, we should first project 3D Gaussian primitives to 2D. Specifically, for a given viewpoint transformation matrix W and a projection matrix K , we can obtain the covariance and the position in 2D space:

$$\begin{aligned} \Sigma^{2D} &= (JW\Sigma W^T J^T)_{1:2,1:2} \\ \mu^{2D} &= K \left(\frac{W\mu}{(W\mu)_z} \right)_{1:2} \end{aligned} \quad (3)$$

where J is the Jacobian of the affine approximation of the projective transformation. And we can get the 2D Gaussian \mathcal{G}^{2d} based on Eq. 1.

After sorting the Gaussian primitives in 2D space based on depth, we can obtain the color of the specified pixel in the image:

$$c(x) = \sum_{i=1}^N c_i \alpha_i \mathcal{G}_i^{2D} \prod_{j=1}^{i-1} (1 - \alpha_j \mathcal{G}_j^{2D}(x)) \quad (4)$$

Here, c_i represents the view-dependent color obtained by combining the SH coefficients of \mathcal{G}_i with the viewing direction.

3.2 4D Volume Representation Based on Hex-planes

Previous works modeling dynamic scenes using plane field encoders mostly employed hexplanes P , which encompass spatial-only planes $P_{so} = \{P_{x,y}, P_{y,z}, P_{x,z}\}$ and spatiotemporal planes $P_{st} = \{P_{x,t}, P_{y,t}, P_{z,t}\}$. Each plane $P_{i,j}$ in P is a $M \times N \times N$ two-dimensional grid, where M represents the feature dimension and N represents the spatiotemporal resolution of the grid. For a 4D sample point $q = (x,y,z,t)$, we perform interpolation based on its projected coordinates on the six grids to obtain the corresponding feature for this point:

$$\begin{aligned} f(q) &= \prod_{i,j \in C} \psi_{bi}(\pi_{i,j}(q); P_{i,j}) \\ C &= \{(x, y), (x, z), (x, t), (y, z), (y, t), (z, t)\} \end{aligned} \quad (5)$$

Here, $f(q)$ is an M -dimensional feature, ψ_{bi} represents bilinear interpolation, and $\pi_{i,j}(q)$ denotes the projected coordinates of sample point q on $P_{i,j}$.

4 METHOD

In this section, we initiate with the presentation of overall pipeline of SaRO-GS in Sec. 4.1. Subsequently, we explore the Scale-aware Residual Field in Sec. 4.2, with a particular emphasis on its consideration of scale information for Gaussian primitives. Following this, we elaborate on the Adaptive Optimization strategy employed in

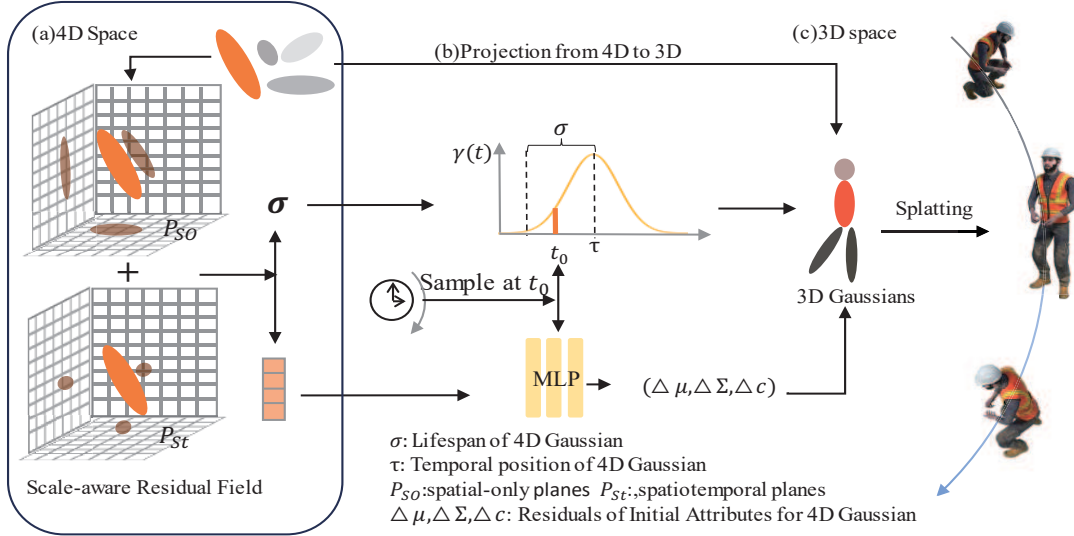


Figure 2: The overall pipeline of SaRO-GS. (a) In 4D space, we simultaneously optimize a set of 4D Gaussians and a scale-aware Residual Field \mathcal{M} . When combined with \mathcal{M} , each Gaussian generates a residual feature and a lifespan σ . They both represent the temporal characteristics of the Gaussian primitive. (b) Given a sampling time t_0 , we can compute the survival status $\gamma(t_0)$ of the Gaussian and decode the residual feature of the Gaussian at time t_0 using an MLP, yielding residual of attributes. Finally, we combine these residuals with the initial attributes of the Gaussian in 4D space to get the 3D Gaussian representation. (c) Once we obtain the representation of the 3D Gaussian, we can generate rendered images using Gaussian Splatting.

Sec. 4.3. Finally, we delineate the loss function and regularization terms utilized in our approach in Sec. 4.4.

4.1 Representation of SaRO-GS

To represent a dynamic scene, we utilize a set of Gaussian primitives \mathcal{G}^{4D} in 4D space alongside Scale-aware Residual Field \mathcal{M} , as shown in Fig. 2(a). Each 4D Gaussian primitive \mathcal{G}_i^{4D} possesses a temporal position τ_i , it is learned alongside its 3D position (x, y, z) , forming a 4D location $\mu^{4D} = (x, y, z, \tau)$. Together with the initial attributes Σ^{4D} , c^{4D} and α^{4D} , a 4D Gaussian primitive and its residual feature f can be represented as follows:

$$\mathcal{G}^{4D} = (\mu^{4D}, \Sigma^{4D}, c^{4D}, \alpha^{4D}), \quad (6)$$

$$f = \mathcal{M}(\mathcal{G}^{4D}). \quad (7)$$

Σ^{4D} , c^{4D} and α^{4D} respectively represent the initial covariance, color, and opacity of the Gaussian primitive in 4D space. Similar to 3D Gaussian, we employ quaternion rotation $q^{4D} = (q_a, q_b, q_c, q_d)$ and scaling vectors $s^{4D} = (s_x, s_y, s_z)$ to represent covariance, and utilize SH (Spherical Harmonics) coefficients to depict view-dependent color.

To address complex temporal scenarios such as object appearance and disappearance, each Gaussian primitive should have a lifespan to indicate how long it can survive in the temporal domain. In order to effectively integrate the Scale-aware Residual Field \mathcal{M} with our 4D Gaussian primitives and leverage the spatiotemporal characteristics of \mathcal{M} , we employ a tiny MLP \mathcal{F}_w to perform inference on f_i and compute the lifespan σ_i of \mathcal{G}_i^{4D} :

$$\sigma_i = \mathcal{F}_w(f_i) = \mathcal{F}_w(\mathcal{M}(\mathcal{G}_i^{4D})). \quad (8)$$

Therefore, in our 4D space, each Gaussian primitive \mathcal{G}_i^{4D} can obtain a residual feature f_i and a lifespan σ_i through \mathcal{M} . $\{\mathcal{G}_i^{4D}, f_i, \sigma_i\}$ fully

represents both the initial attributes and temporal characteristics of a Gaussian primitive in 4D space.

Once the sampling time t_0 are given, we need to project the Gaussian primitives from 4D space to 3D space, as shown in Fig. 2(b). We first need to examine whether \mathcal{G}_i^{4D} still survives at the current sampling time t_0 . Inspired by [27], we adopt a Gaussian-like state function $\gamma(t)$ to model the state of \mathcal{G}_i^{4D} as it varies with the sampling time t :

$$\gamma_i(t) = e^{-k \frac{t - \tau_i}{\sigma_i}}. \quad (9)$$

Where t represents the sampling time, and τ_i represents the temporal position of \mathcal{G}_i^{4D} . In practice, k is set to 4. As the sampling time t gradually moves away from the temporal position of \mathcal{G}_i^{4D} , $\gamma(t)$ decreases from 1. When the sampling time reaches the Gaussian lifespan σ_i , $\gamma(t)$ will decrease to 0.01, indicating that \mathcal{G}_i^{4D} is nearly inactive at t , which means it should be invisible when projected into 3D space. So for a given sampling time t_0 , We can utilize this state function to represent the opacity of \mathcal{G}_i^{4D} in 3D space after projection:

$$\alpha_i^{3D} = \alpha_i^{4D} \times \gamma_i(t_0) \quad (10)$$

Apart from opacity, other features of \mathcal{G}_i^{4D} also vary with sampling time t when projected into 3D space. We can utilize a set of MLPs \mathcal{F}_θ to decode the residual feature f_i of \mathcal{G}_i^{4D} at the sampling time t , thereby obtaining the residual of the projected attributes as they vary with the sampling time t .

$$\Delta \mu_i(t), \Delta \Sigma_i(t), \Delta c_i(t) = \mathcal{F}_\theta(f(\mathcal{G}_i^{4D}), t - \tau_i) \quad (11)$$

$\Delta \mu_i(t)$, $\Delta \Sigma_i(t)$ and $\Delta c_i(t)$ respectively represent the residuals of position, covariance, and color. Here we decode using $t - \tau_i$ instead of just t , as we aim to obtain the residual relative to the initial attribute of \mathcal{G}_i^{4D} in 4D space, where \mathcal{G}_i^{4D} is temporally positioned using τ_i .

Therefore, we can obtain the attributes of projected \mathcal{G}_i^{3D} at a given time t_0 :

$$\mu_i^{3D} = \mu_i^{4D}[:3] + \Delta\mu_i(t_0), \quad (12)$$

$$\Sigma_i^{3D} = \Sigma_i^{4D} + \Delta\Sigma_i(t_0), \quad (13)$$

$$c_i^{3D} = c_i^{4D} + \Delta c_i(t_0). \quad (14)$$

$\mu_i^{4D}[:3]$ represents extracting the xyz components of μ_i^{4D} as the initial 3D location, and $\Delta\Sigma_i$ can be decomposed into $\Delta\Sigma_i[:3]$ and $\Delta\Sigma_i[3:]$, representing the residuals of the three-dimensional scaling vector and quaternion rotation about \mathcal{G}_i^{4D} , respectively. The changes to Σ_i^{4D} and c_i^{4D} are achieved by adjusting the corresponding quaternion rotation, scaling vectors, and SH coefficients.

Therefore, according to Eq. [8-14], Gaussian primitives in 4D space evolve within their lifespan as the sampling time varies, projecting into 3D space at a given sampling time. Then, based on Eq. 34, we employ 3DGS to render 3D Gaussians, obtaining rendered images from a given camera viewpoint, as shown in Fig. 2(c).

4.2 Scale-aware Residual Field

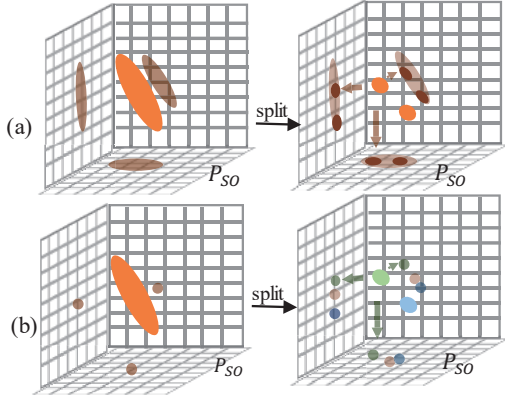


Figure 3: The impact of scale is not taken into account in Gaussian self-splitting. (a)When size information is considered, the features of the split Gaussian remain similar to its parent Gaussian. (b)Otherwise, the split Gaussian will have features different from its parent Gaussian

To fully integrate the spatiotemporal information of the scene and save computational resources, we adopt hexplanes to represent our Scale-aware Residual Field \mathcal{M} , which consists of spatial-only planes and spatiotemporal planes, as described in Sec. 3.2.

However, neglecting the size of Gaussian primitives and solely projecting them onto planes based on their 4D positions for feature extraction would lead to incorrect residual features. First, Gaussian primitives can be approximated as ellipsoids. Therefore, when projecting a Gaussian primitive onto a spatial-only plane, we obtain an elliptical region instead of a single point, as in the current NeRF-based approach. Thus, the corresponding feature for a Gaussian primitive should be a combination of all the areas it occupies in the plane. Secondly, if we follow the self-splitting strategy of 3DGS and split a large Gaussian primitive into smaller ones, they would have different residual features, significantly deviating from those of their parent primitive, which contradicts our original intention, as shown in Fig. 3. So, finding an appropriate method to encode the region projected by Gaussian is crucial.

We propose a scale-aware Residual Field to address the aforementioned issue, which decompose the 4D space into three spatial-only planes P_{so} and three spatiotemporal planes P_{st} . Given that the size of Gaussian primitives impacts their projection only within the spatial-only plane P_{so} , we specifically consider only employing scale-aware encoding within them, as shown in Fig. 2.

For every spatial-only planes $P_{i,j}$, we employ a MipMap stack to represent features at different spatial scales in the scene. The level 0 of the MipMap stack $P_{i,j}^0$ is a feature map with shape $M \times N \times N$, which has the smallest spatial scale s^0 among all levels. And remaining levels $P_{i,j}^l$ in the Mipmap stack are obtained by computing thumbnails based on the features of the previous level, where the width and height are reduced by a factor of 2 each. Taking $P_{x,y}$ as an example, the relationship between their spatial scale is as follows:

$$\begin{aligned} s_x^0 &= \frac{\mathcal{B}_{max}^x - \mathcal{B}_{min}^x}{N} & s_y^0 &= \frac{\mathcal{B}_{max}^y - \mathcal{B}_{min}^y}{N} \\ s^{l+1} &= 2 \times s^l & l &\in [0, L-1] \end{aligned} \quad (15)$$

The variables \mathcal{B}_{max} and \mathcal{B}_{min} respectively represent the maximum and minimum values of the scene’s bounding box and s^l is the spatial scale of level l in the MipMap stack. In practice, we only store and optimize the features in level 0 MipMap $P_{x,y}^0$, while the remaining levels are dynamically computed and generated during forward inference. This way, we possess the capability to encode features at different spatial scales within the scene.

Meanwhile, for a Gaussian primitive with a scaling s in 4D space, when projected onto the spatial-only plane $P_{x,y}$, it results in a 2D ellipse with axes (s_x, s_y) . Therefore, based on the projected axes of the Gaussian primitive on $P_{x,y}$ and the corresponding base spatial scale $s_{x,y}^0$ of the MipMap stack, we can determine the spatial scale level associated with this Gaussian primitive:

$$l^x = \log_2\left(\frac{s_x}{s_x^0}\right) \quad l^y = \log_2\left(\frac{s_y}{s_y^0}\right) \quad (16)$$

To maintain the highest possible accuracy, we choose the minimum value among them as the final spatial level $l = \min(l^x, l^y)$. So now we can obtain the two MipMap features that are closest to its spatial level: $P_{x,y}^{[l]}$, $P_{x,y}^{[l+1]}$, and we can obtain the embedding of the Gaussian primitive with 4D position μ_{4d} in $P_{x,y}$ as:

$$f_{x,y} = \psi_{tri}(\pi_{x,y}(\mu_{4d}), l; P_{x,y}^{[l]}, P_{x,y}^{[l+1]}), \quad (17)$$

Here, ψ_{tri} represents trilinear interpolation in the space formed by $P_{x,y}^{[l]}$ and $P_{x,y}^{[l+1]}$. The complete expression of the scale-aware residual feature f of \mathcal{G}^{4D} is as follows:

$$\begin{aligned} f(\mathcal{G}^{4D}) &= f_{so} + f_{st} \\ &= \sum_{i,j \in C_{so}} \psi_{tri}(\pi_{x,y}(\mu^{4D}), l; P_{x,y}^{[l]}, P_{x,y}^{[l+1]}) + \\ &\quad \sum_{i,j \in C_{st}} \psi_{bi}(\pi_{i,j}(\mu^{4D}); P_{i,j}) \end{aligned} \quad (18)$$

$$C_{so} = \{(x, y), (x, z), (y, z)\} \quad C_{st} = \{(x, t), (y, t), (z, t)\}.$$

Here, ψ_{tri}, ψ_{bi} represent trilinear interpolation and bilinear interpolation respectively. Through experiments, we found that summation is a more effective way to combine features in our Scale-aware Residual Field compared to others.

4.3 Adaptive Optimization

Due to the varying temporal properties of Gaussian primitives in this 4D space, each Gaussian primitive is sampled with different probabilities over observed time. Dynamic primitives, in order to represent the temporal complexity of the scene, often have a smaller lifespan, resulting in a lower sampling probability compared to static primitives. These dynamic primitives would have smaller gradients during the backward propagation of the loss function. The gradient value is crucial in the 3DGS framework, as it needs to exceed a threshold to densify the corresponding primitive and optimize the currently imperfectly reconstructed regions. Hence, applying the same optimization and densification strategy directly to each primitive with 3DGS[22] may lead to optimization imbalance.

To tackle the aforementioned issue, we propose an Adaptive Optimization strategy, which dynamically adjusts the learning rate and densify gradient threshold for \mathcal{G}_i^{4D} based on its sampling probability across the observable time range. Specifically, We can use $\gamma_i(t)$ of \mathcal{G}_i^{4D} to calculate the temporal integral within the observable range, representing its sampling probability. The larger the integral, the more the Gaussian primitive’s lifespan intersects with the observable range, making it more likely to be sampled.

Definite Integral of the Time Domain Distribution. Based on state function $\gamma_i(t)$ of \mathcal{G}_i^{4D} , we can compute its integral over the time domain.

$$F(t) = P(x < t) = \int_{-\infty}^t e^{-k \frac{x-\tau_i}{\sigma_i}} dx \quad (19)$$

$$I = F(t_{end}) - F(t_{start}) \quad (20)$$

$F(t)$ represents the CDF (cumulative distribution function) of each Gaussian primitive. Here, I denotes the definite integral over the entire time domain from t_{start} to t_{end} , where t_{start} and t_{end} normalize to 0 and 1, respectively.

Since $\gamma_i(t)$ is a Gaussian-like function, it is challenging to compute precise definite integral values. Inspired by [35], we derive the approximate cumulative distribution function as:

$$Q(t) = \int_{-\infty}^t \frac{1}{\sqrt{2\pi}} e^{-\frac{x^2}{2}} dx = 1 - \frac{1}{e^{1+\alpha_1 t^3 + \alpha_2 t}} \quad (21)$$

$$F(t) = \frac{\sqrt{\pi}\sigma_i}{\sqrt{k}} Q(\sqrt{2k} \frac{(t - \tau_i)}{\sigma_i}) \quad (22)$$

Here, $\alpha_1 = 0.070565992$, $\alpha_2 = 1.5976$. Please refer to the appendix for details. Therefore, we can obtain the definite integral of Gaussian primitives over the time domain using Eq. 20 with minimal computational complexity.

Integral-based Per-Gaussian Optimization Schedule. After get the temoral intergral of each Gaussian, we can dynamically adjust the learning rates and gradient thresholds for densification control on a per-primitive basis, aiming to achieve rapid reconstruction of dynamic regions:

$$\kappa_i = \kappa_{base} * \frac{I_i}{I_{max}}, \quad lr_i = lr_{base} * \frac{I_{max}}{I_i} \quad (23)$$

Here, κ_i and lr_i respectively represent the densification threshold and the learning rate of \mathcal{G}_i^{4D} , while I_i and I_{max} respectively denote the timeporal integral of \mathcal{G}_i^{4D} and the maximum time-domain integral among all Gaussian primitives. We adjust its densification threshold each time densification control is required. Additionally, for the learning rate, we dynamically adjust it every 50 iterations based on Eq. 23, involving parameters related to 4D position, scaling, rotation, and zeroth-order SH coefficients of \mathcal{G}_i^{4D} .

4.4 Loss Function

Regularization term for scaling residuals: When the sampling time t equals the temporal position of \mathcal{G}_i^{4D} , we aim for minimal variations in the attributes of Gaussian primitives projected into 3D space compared to their initial values in 4D space. Excessive reliance on attribute residuals during the projection process may neglect the optimization of their initial values. Additionally, we strive to minimize the disparity between the initial scaling values of Gaussian primitives in 4D space and their values in 3D space. This ensures that the Scale-aware Residual Field can effectively integrate accurate scale information. To achieve this goal, we propose a regularization term \mathcal{L}_{SR} concerning scaling residuals:

$$\mathcal{L}_{SR}(\mathcal{G}^{4D}) = \frac{1}{n} \sum_i \|\Delta\Sigma_i(\tau_i)[:3]\|_2 \quad (24)$$

Here, $\Delta\Sigma_i(\tau_i)[:3]$ represents the residuals of scaling of \mathcal{G}_i^{4D} obtained during the projection process when the sampling time is \mathcal{G}_i^{4D} ’s temporal position τ_i , where n is the total number of Gaussian primitives in the current 4D space.

Total Loss Function Following [22], we use the loss between the rendered image and the ground truth image, which includes an \mathcal{L}_1 term and a \mathcal{L}_{D-SSIM} term. Combined with our regularization terms, the overall loss function is formulated as:

$$\mathcal{L} = (1 - \lambda_1)\mathcal{L}_1 + \lambda_1\mathcal{L}_{D-SSIM} + \lambda_2\mathcal{L}_{SR} \quad (25)$$

The settings for λ_1 and λ_2 can be referred to in Sec. 5.

5 IMPLEMENTATION DETAILS

We implemented our work using the PyTorch[37] framework and open-source code based on 3DGS. We utilized the nvidiffrast[23] library to compute the MipMap stack in the Scale-aware Residual Field, ensuring computational efficiency. We use Adam optimizer and retained certain implementations from 3DGS, including the fast differentiable rasterizer, hyperparameters, and opacity reset strategy. In the loss function Eq. 25, we set λ_1 to 0.2 and λ_2 to 0.8. We conducted training and testing using a single RTX 3090.

To enhance our rendering speed, we adopted a lossless baking strategy for the model during rendering. During rendering, we can pre-compute the features for each Gaussian primitive in the 4D space and for a given sampling time t_0 , we filter out points where the survival status $\gamma(t_0) < 0.001$. These filtered points indicate that they are inactive and invisible at time t_0 , thereby reducing the computational overhead during MLP Decoder and Splatting. After testing, our baking strategy has enabled us to double our rendering speed. Please refer to the appendix for more details.

Table 1: Quantitative results on the monocular synthesis dataset D-NeRF. FPS is measured at 400×400 . † denotes a dynamic Gaussian method. The evaluation of ¹ is conducted at a resolution of 800, while the remaining methods are evaluated at 400

Method	PSNR(dB)†	SSIM†	LPIPS↓	FPS†	Train Time
D-NeRF[42]	29.67	0.95	0.07	0.06	48h
KPlanes-hybrid[13]	32.36	0.96	-	0.97	52m
TiNeuVox-B[12]	32.67	0.97	0.04	1.5	28m
V4D[15]	33.72	0.98	0.02	2.08	6.9h
HexPlane[7]	31.04	0.97	0.04	2.5	11m 30s
4DGS[61]† ¹	34.05	0.98	0.02	82	20m
4DGS-Realtime[65]†	34.09	0.98	-	-	-
Ours	36.13	0.98	0.01	182.29	45m

Table 2: Quantitative results on the monocular synthesis dataset D-NeRF at more resolutions.

Method	PSNR(dB)†	FPS†	Method	PSNR(dB)†	FPS†
4DGS(400x400)	35.05	107	4DGS(800x800)	34.05	82
Ours(400x400)	36.13	182	Ours(800x800)	35.24	149



Figure 4: Qualitative result on the D-NeRF dataset.

6 EXPERIMENTS

6.1 Datasets

Synthetic Dataset. We chose D-NeRF[42] as our evaluation dataset for monocular scenes. D-NeRF is a monocular synthetic dataset consisting of eight scenes with large-scale movements and real non-Lambertian material dynamic objects, which imposes a challenge on model performance.

Real-world Datasets. We selected Plenoptic Video dataset[26] to evaluate our performance in multi-view real dynamic scenes. Plenoptic Video dataset consists of six real-world scenes, each captured by 15-20 cameras. Each scene in the dataset encompasses complex movements and occurrences of object appearance and disappearance. This dataset allows for a comprehensive evaluation of the model’s reconstruction capability in complex temporal scenes.

6.2 Results

We have employed a variety of evaluation metrics to assess our model. For rendering quality, we utilize PSNR, SSIM, DSSIM, and LPIPS, and for rendering speed, we measure FPS. All evaluation results are averaged across all scenes in the dataset.

For monocular scenes in the D-NeRF dataset, we compare our method against the current state-of-the-art methods[7, 12, 13, 15, 42, 61, 65] in the field. The quantitative evaluation results are listed in Tab. D1.2. The dynamic scene representation method based on NeRF[7, 12, 13, 15, 42] struggles with achieving real-time rendering

Table 3: Quantitative results on Plenoptic Video dataset. FPS is measured at 1352×1014 . † denotes a dynamic Gaussian method.¹: excludes the Coffee Martini scene. ²: Only report SSIM instead of MS-SSIM like others.

Method	PSNR(dB)†	DSSIM↓	LPIPS↓	FPS
KPlanes-hybrid[13]	31.63	-	-	0.3
Mix-Voxels-L[57]	31.34	0.017	0.096	16.7
NeRFPlayer[51]	30.69	0.034 ²	0.111	0.045
HyperReel[2]	31.1	0.037 ²	0.096	2.00
StreamRF[25]	31.04	-	0.040	8.3
HexPlane[7] ¹	31.71	0.014	0.075	-
4DGS-Realtime[65]†	32.01	0.014	-	114
Spacetime-Gs[27]†	32.05	0.014	0.044	140
4DGS[61]†	31.15	0.016	0.049	30
Ours	32.15	0.014	0.044	40

Table 4: The ablation study results across all scenes in the D-NeRF dataset.

Method	PSNR(dB)†	SSIM†
No Scale-aware	35.61	0.98
No temporal prop.	32.29	0.96
No Adaptive Optimization	35.44	0.98
No res-Reg.	35.43	0.98
Full	36.13	0.98

due to the need for dense ray sampling during rendering. However, our method achieves a rendering speed of 182 FPS and exhibits considerable improvement in rendering quality. Compared to existing dynamic Gaussian methods[61, 65], our approach demonstrates superior performance in handling complex temporal scenes and achieves a certain level of enhancement in rendering quality. Qualitative comparison results can be seen in Fig. 4. In the standup scene, our method demonstrates better reconstruction of details (such as facial and hand features).

For multi-view scenes in the Plenoptic Video dataset, our evaluation results are presented in Tab. D2. As mentioned in [27, 65], there are two different calculation settings for DSSIM in previous works, and we have indicated this in the table. Our method outperforms all compared methods in rendering quality while maintaining superior rendering speed, achieving real-time rendering. The NeRF-based methods[2, 7, 13, 25, 51, 57] have a significant disadvantage in rendering speed compared to ours. 4DGS[61] based on deformation fields has shortcomings in modeling complex temporal situations such as object appearance and disappearance, which we can effectively address. Although Spacetime-GS[27] achieves higher rendering speeds, it is only applicable to multi-view scenes, whereas our method is suitable for both multi-view and single-view scenarios. A qualitative comparison of rendering quality with Gaussian methods can be seen in Fig. 5. Our approach demonstrates more accurate reconstructions in temporally complex scenes (such as the inverted coffee scene with details on the heads and hands) and richer details (such as the circular decorations on the upper garment and reflections on the clippers in the cut beef scene).

6.3 Ablation Study

Temporal properties of 4D Gaussian. Each Gaussian in 4D space possesses temporal properties, including temporal position and lifespan, giving us an advantage over previous deformation-based



Figure 5: Qualitative results on coffee martinis and cut roasted beef from the Plenoptic Video dataset

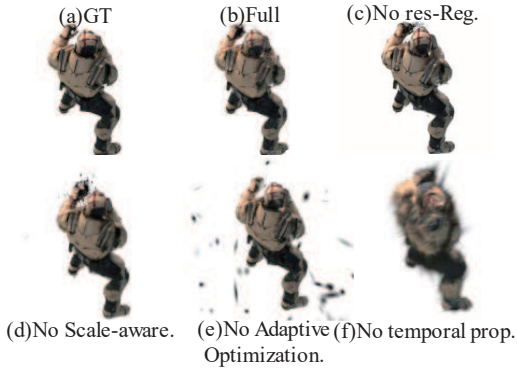


Figure 6: Qualitative results of the ablation study.

methods in handling intricate temporal information. To demonstrate this, we fix the temporal position of each point to frame 0 and enable Gaussians to traverse the entire sampling time. The results, as presented in Tab. 4 and Fig. 6, show a notable decline in performance when temporal position and lifespan are disregarded. **Consideration of Spatial Scale in the Residual Field.** In our Residual field, we take into account the size information of each Gaussian, improving the accuracy of the residual features. To evaluate this approach, we refrain from encoding the projection area in spatial-only planes. As depicted in Tab. 4 and Fig. 6, not incorporating the size information of Gaussian primitives results in a reduction in the reconstruction quality of dynamic scenes.

Adaptive Optimization. To address the imbalance in optimization between dynamic and static regions in the scene, we introduce the Adaptive Optimization strategy. Without this strategy, the reconstruction ability of 4D Gaussians for moving regions would decrease. This is supported by Tab. 4. Without this strategy, Gaussian primitives struggle to distinguish between dynamic and static regions, leading to artifacts as shown in Fig. 6(e).

Regularization of scaling residuals. We conducted evaluations without regularization of scaling residuals to validate the effectiveness of this regularization term. Without this constraint, Gaussian primitives overly rely on the Scale-aware Residual field, neglecting optimization of their own initial attributes, resulting in a decrease in model performance, as shown in Tab. 4 and Fig. 6.

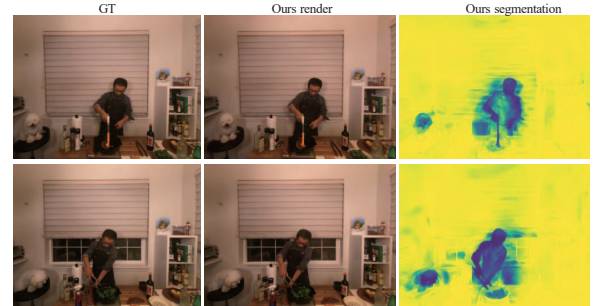


Figure 7: Segmentation of dynamic and static scenes.

6.4 Limitations

Our method achieves high-quality, real-time reconstruction of temporally complex scenes. However, it has limitations, the use of explicit and implicit mixing, such as 4D space plane decomposition and MLP inference, may reduce training speed. Furthermore, there are many possible extensions to explore based on SaRO-GS, such as 4D content generation[68], dynamic object tracking[31], and combining with Large Language Models[1] or Spoken Language Understanding[9, 10, 48] to achieve more flexible interaction modes.

6.5 Dynamic-Static segmentation

Static primitives are observable throughout the entire observation period, whereas dynamic primitives are only visible near their temporal positions. Therefore, dynamic primitives have a shorter lifespan, while static primitives have a much longer lifespan. Consequently, we can segment the scene into dynamic and static parts based solely on their lifespans, as illustrated in Fig. 7. Our method accurately segments dynamic foreground elements and dynamic lighting effects (e.g., shadows of people in the image). This aspect also underscores the interpretability of our method.

7 CONCLUSION

In this paper, we propose SaRO-GS as a novel approach for representing dynamic scenes, enabling real-time rendering while ensuring high-quality reconstruction, especially in temporally complex scenes. SaRO-GS utilizes a set of 4D Gaussians to represent dynamic scenes and leverages 3D Gaussian Splatting for real-time rendering. Additionally, we propose a Scale-aware Residual Field to encode the

region occupied by Gaussian primitives, resulting in more accurate features and align with the self-splitting behavior of Gaussians. Furthermore, we introduce an Adaptive Optimization strategy to enhance the model's ability to reconstruct high-frequency temporal information in dynamic scenes. Experimental results in both monocular and multi-view settings demonstrate that SaRO-GS achieves SOTA rendering quality while enabling real-time rendering.

Acknowledgments

This work is financially supported by Guangdong Provincial Key Laboratory of Ultra High Definition Immersive Media Technology, this work is also financially supported for Outstanding Talents Training Fund in Shenzhen, Shenzhen Science and Technology Program-Shenzhen Cultivation of Excellent Scientific and Technological Innovation Talents project(Grant No. RCJC20200714114435057) , R24115SG MIGU-PKU META VISION TECHNOLOGY INNOVATION LAB.

References

- [1] Josh Achiam, Steven Adler, Sandhini Agarwal, Lama Ahmad, Ilge Akkaya, Florencia Leoni Aleman, Diogo Almeida, Janko Altenschmidt, Sam Altman, Shyamal Anadkat, et al. 2023. Gpt-4 technical report. *arXiv preprint arXiv:2303.08774* (2023).
- [2] Benjamin Attal, Jia-Bin Huang, Christian Richardt, Michael Zollhoefer, Johannes Kopf, Matthew O'Toole, and Changil Kim. 2023. HyperReel: High-fidelity 6-DoF video with ray-conditioned sampling. In *Proceedings of the IEEE/CVF Conference on Computer Vision and Pattern Recognition*. 16610–16620.
- [3] Yanqi Bao, Yuxin Li, Jing Huo, Tianyu Ding, Xinyue Liang, Wenbin Li, and Yang Gao. 2023. Where and how: Mitigating confusion in neural radiance fields from sparse inputs. In *Proceedings of the 31st ACM International Conference on Multimedia*. 2180–2188.
- [4] Jonathan T Barron, Ben Mildenhall, Matthew Tancik, Peter Hedman, Ricardo Martin-Brualla, and Pratul P Srinivasan. 2021. Mip-nerf: A multiscale representation for anti-aliasing neural radiance fields. In *Proceedings of the IEEE/CVF International Conference on Computer Vision*. 5855–5864.
- [5] Jonathan T Barron, Ben Mildenhall, Dor Verbin, Pratul P Srinivasan, and Peter Hedman. 2022. Mip-nerf 360: Unbounded anti-aliased neural radiance fields. In *Proceedings of the IEEE/CVF Conference on Computer Vision and Pattern Recognition*. 5470–5479.
- [6] Jonathan T Barron, Ben Mildenhall, Dor Verbin, Pratul P Srinivasan, and Peter Hedman. 2023. Zip-nerf: Anti-aliased grid-based neural radiance fields. In *Proceedings of the IEEE/CVF International Conference on Computer Vision*. 19697–19705.
- [7] Ang Cao and Justin Johnson. 2023. Hexplane: A fast representation for dynamic scenes. In *Proceedings of the IEEE/CVF Conference on Computer Vision and Pattern Recognition*. 130–141.
- [8] Zhang Chen, Zhong Li, Liangchen Song, Lele Chen, Jingyi Yu, Junsong Yuan, and Yi Xu. 2023. Neurf: A neural fields representation with adaptive radial basis functions. In *Proceedings of the IEEE/CVF International Conference on Computer Vision*. 4182–4194.
- [9] Xuxin Cheng, Bowen Cao, Qichen Ye, Zhihong Zhu, Hongxiang Li, and Yuexian Zou. 2023. Ml-lmcl: Mutual learning and large-margin contrastive learning for improving asr robustness in spoken language understanding. *arXiv preprint arXiv:2311.11375* (2023).
- [10] Xuxin Cheng, Zhihong Zhu, Bowen Cao, Qichen Ye, and Yuexian Zou. 2023. Mrrl: Modifying the reference via reinforcement learning for non-autoregressive joint multiple intent detection and slot filling. In *Findings of the Association for Computational Linguistics: EMNLP 2023*. 10495–10505.
- [11] David Eigen, Christian Puhrsch, and Rob Fergus. 2014. Depth map prediction from a single image using a multi-scale deep network. *Advances in neural information processing systems* 27 (2014).
- [12] Jieming Fang, Taoran Yi, Xinggang Wang, Lingxi Xie, Xiaopeng Zhang, Wenyu Liu, Matthias Nießner, and Qi Tian. 2022. Fast dynamic radiance fields with time-aware neural voxels. In *SIGGRAPH Asia 2022 Conference Papers*. 1–9.
- [13] Sara Fridovich-Keil, Giacomo Meanti, Frederik Rahbæk Warburg, Benjamin Recht, and Angjoo Kanazawa. 2023. K-planes: Explicit radiance fields in space, time, and appearance. In *Proceedings of the IEEE/CVF Conference on Computer Vision and Pattern Recognition*. 12479–12488.
- [14] Sara Fridovich-Keil, Alex Yu, Matthew Tancik, Qinhong Chen, Benjamin Recht, and Angjoo Kanazawa. 2022. Plenoxels: Radiance fields without neural networks. In *Proceedings of the IEEE/CVF Conference on Computer Vision and Pattern Recognition*. 5501–5510.
- [15] Wanshui Gan, Hongbin Xu, Yi Huang, Shifeng Chen, and Naoto Yokoya. 2023. V4d: Voxel for 4d novel view synthesis. *IEEE Transactions on Visualization and Computer Graphics* (2023).
- [16] Huachen Gao, Xiaoyu Liu, Meixia Qu, and Shijie Huang. 2021. Pdanet: Self-supervised monocular depth estimation using perceptual and data augmentation consistency. *Applied Sciences* 11, 12 (2021), 5383.
- [17] Ravi Garg, Vijay Kumar Bg, Gustavo Carneiro, and Ian Reid. 2016. Unsupervised cnn for single view depth estimation: Geometry to the rescue. In *Computer Vision—ECCV 2016: 14th European Conference, Amsterdam, The Netherlands, October 11–14, 2016, Proceedings, Part VIII 14*. Springer, 740–756.
- [18] Xiang Guo, Jiadai Sun, Yuchao Dai, Guanying Chen, Xiaoqing Ye, Xiao Tan, Errui Ding, Yumeng Zhang, and Jingdong Wang. 2023. Forward flow for novel view synthesis of dynamic scenes. In *Proceedings of the IEEE/CVF International Conference on Computer Vision*. 16022–16033.
- [19] Peter Hedman, Pratul P Srinivasan, Ben Mildenhall, Jonathan T Barron, and Paul Debevec. 2021. Baking neural radiance fields for real-time view synthesis. In *Proceedings of the IEEE/CVF International Conference on Computer Vision*. 5875–5884.
- [20] Wenbo Hu, Yuling Wang, Lin Ma, Bangbang Yang, Lin Gao, Xiao Liu, and Yuewen Ma. 2023. Tri-miprf: Tri-mip representation for efficient anti-aliasing neural radiance fields. In *Proceedings of the IEEE/CVF International Conference on Computer Vision*. 19774–19783.
- [21] Yi-Hua Huang, Yang-Tian Sun, Ziyi Yang, Xiaoyang Lyu, Yan-Pei Cao, and Xiaojuan Qi. 2023. SC-GS: Sparse-Controlled Gaussian Splatting for Editable Dynamic Scenes. *arXiv preprint arXiv:2312.14937* (2023).
- [22] Bernhard Kerbl, Georgios Kopanas, Thomas Leimkühler, and George Drettakis. 2023. 3d gaussian splatting for real-time radiance field rendering. *ACM Transactions on Graphics (ToG)* 42, 4 (2023), 1–14.
- [23] Samuli Laine, Janne Hellsten, Tero Karras, Yeongho Seol, Jaakko Lehtinen, and Timo Aila. 2020. Modular primitives for high-performance differentiable rendering. *ACM Transactions on Graphics (ToG)* 39, 6 (2020), 1–14.
- [24] Jiahe Li, Jiawei Zhang, Xiao Bai, Jin Zheng, Xin Ning, Jun Zhou, and Lin Gu. 2024. DNGaussian: Optimizing Sparse-View 3D Gaussian Radiance Fields with Global-Local Depth Normalization. *arXiv preprint arXiv:2403.06912* (2024).
- [25] Lingzhi Li, Zhen Shen, Zhongshu Wang, Li Shen, and Ping Tan. 2022. Streaming radiance fields for 3d video synthesis. *Advances in Neural Information Processing Systems* 35 (2022), 13485–13498.
- [26] Tianye Li, Mira Slavcheva, Michael Zollhoefer, Simon Green, Christoph Lassner, Changil Kim, Tanner Schmidt, Steven Lovegrove, Michael Goesele, and Richard Newcombe. 2022. Neural 3d video synthesis from multi-view video. In *Proceedings of the IEEE/CVF Conference on Computer Vision and Pattern Recognition*. 5521–5531.
- [27] Zhan Li, Zhang Chen, Zhong Li, and Yi Xu. 2023. Spacetime Gaussian Feature Splatting for Real-Time Dynamic View Synthesis. *arXiv:2312.16812* pages. <https://doi.org/10.48550/arXiv.2312.16812> Project page: <https://oppo-us-research.github.io/SpacetimeGaussians-website/>.
- [28] Haotong Lin, Sida Peng, Zhen Xu, Tao Xie, Xingyi He, Hujun Bao, and Xiaowei Zhou. 2023. High-fidelity and real-time novel view synthesis for dynamic scenes. In *SIGGRAPH Asia 2023 Conference Papers*. 1–9.
- [29] Jia-Wei Liu, Yan-Pei Cao, Weijia Mao, Wenqiao Zhang, David Junhao Zhang, Jussi Keppo, Ying Shan, Xiaohu Qie, and Mike Zheng Shou. 2022. Devrf: Fast deformable voxel radiance fields for dynamic scenes. *Advances in Neural Information Processing Systems* 35 (2022), 36762–36775.
- [30] David G Lowe. 2004. Distinctive image features from scale-invariant keypoints. *International journal of computer vision* 60 (2004), 91–110.
- [31] Jonathon Luiten, Georgios Kopanas, Bastian Leibe, and Deva Ramanan. 2023. Dynamic 3d gaussians: Tracking by persistent dynamic view synthesis. *arXiv preprint arXiv:2308.09713* (2023).
- [32] Ben Mildenhall, Pratul P Srinivasan, Matthew Tancik, Jonathan T Barron, Ravi Ramamoorthi, and Ren Ng. 2021. Nerf: Representing scenes as neural radiance fields for view synthesis. *Commun. ACM* 65, 1 (2021), 99–106.
- [33] Thomas Müller, Alex Evans, Christoph Schied, and Alexander Keller. 2022. Instant neural graphics primitives with a multiresolution hash encoding. *ACM Transactions on Graphics* 41, 4 (2022), 1–15. <https://doi.org/10.1145/3528223.3530127>
- [34] Michael Niemeyer, Jonathan T Barron, Ben Mildenhall, Mehdi SM Sajjadi, Andreas Geiger, and Noha Radwan. 2022. Regnerf: Regularizing neural radiance fields for view synthesis from sparse inputs. In *Proceedings of the IEEE/CVF Conference on Computer Vision and Pattern Recognition*. 5480–5490.
- [35] E. Page. 2018. Approximations to the Cumulative Normal Function and its Inverse for Use on a Pocket Calculator. *Journal of the Royal Statistical Society Series C: Applied Statistics* 26, 1 (2018), 75–76. <https://doi.org/10.2307/2346872>
- [36] Keunhong Park, Utkarsh Sinha, Peter Hedman, Jonathan T Barron, Sofien Bouaziz, Dan B Goldman, Ricardo Martin-Brualla, and Steven M Seitz. 2021. Hypernerf: A higher-dimensional representation for topologically varying neural radiance

- fields. *arXiv preprint arXiv:2106.13228* (2021).
- [37] Adam Paszke, Sam Gross, Francisco Massa, Adam Lerer, James Bradbury, Gregory Chanan, Trevor Killeen, Zeming Lin, Natalia Gimelshein, and Luca Antiga. 2019. Pytorch: An imperative style, high-performance deep learning library. *Advances in neural information processing systems* 32 (2019).
- [38] Rui Peng, Xiaodong Gu, Luyang Tang, Shihe Shen, Fanqi Yu, and Ronggang Wang. 2023. Gens: Generalizable neural surface reconstruction from multi-view images. *Advances in Neural Information Processing Systems* 36 (2023), 56932–56945.
- [39] Rui Peng, Rongjie Wang, Zhenyu Wang, Yawen Lai, and Ronggang Wang. 2022. Rethinking depth estimation for multi-view stereo: A unified representation. In *Proceedings of the IEEE/CVF conference on computer vision and pattern recognition*. 8645–8654.
- [40] Sida Peng, Junting Dong, Qianqian Wang, Shangzhan Zhang, Qing Shuai, Xiaowei Zhou, and Hujun Bao. 2021. Animatable neural radiance fields for modeling dynamic human bodies. In *Proceedings of the IEEE/CVF International Conference on Computer Vision*. 14314–14323.
- [41] Sida Peng, Yuanqing Zhang, Yinghao Xu, Qianqian Wang, Qing Shuai, Hujun Bao, and Xiaowei Zhou. 2021. Neural body: Implicit neural representations with structured latent codes for novel view synthesis of dynamic humans. In *Proceedings of the IEEE/CVF Conference on Computer Vision and Pattern Recognition*. 9054–9063.
- [42] Albert Pumarola, Enric Corona, Gerard Pons-Moll, and Francesc Moreno-Noguer. 2021. D-nerf: Neural radiance fields for dynamic scenes. In *Proceedings of the IEEE/CVF Conference on Computer Vision and Pattern Recognition*. 10318–10327.
- [43] Christian Reiser, Songyou Peng, Yiyi Liao, and Andreas Geiger. 2021. Kilonerf: Speeding up neural radiance fields with thousands of tiny mlps. In *Proceedings of the IEEE/CVF International Conference on Computer Vision*. 14335–14345.
- [44] Christian Reiser, Rick Szeliski, Dor Verbin, Pratul Srinivasan, Ben Mildenhall, Andreas Geiger, Jon Barron, and Peter Hedman. 2023. Merf: Memory-efficient radiance fields for real-time view synthesis in unbounded scenes. *ACM Transactions on Graphics (TOG)* 42, 4 (2023), 1–12.
- [45] Paul-Edouard Sarlin, Daniel DeTone, Tomasz Malisiewicz, and Andrew Rabino-vich. 2020. SuperGlue: Learning feature matching with graph neural networks. In *Proceedings of the IEEE/CVF conference on computer vision and pattern recognition*. 4938–4947.
- [46] Johannes Lutz Schönberger and Jan-Michael Frahm. 2016. Structure-from-Motion Revisited. In *Conference on Computer Vision and Pattern Recognition (CVPR)*.
- [47] Johannes Lutz Schönberger, Enliang Zheng, Marc Pollefeys, and Jan-Michael Frahm. 2016. Pixelwise View Selection for Unstructured Multi-View Stereo. In *European Conference on Computer Vision (ECCV)*.
- [48] Dmitry Serdyuk, Yongqiang Wang, Christian Fuegen, Anuj Kumar, Baiyang Liu, and Yoshua Bengio. 2018. Towards end-to-end spoken language understanding. In *2018 IEEE International Conference on Acoustics, Speech and Signal Processing (ICASSP)*. IEEE, 5754–5758.
- [49] Ruizhi Shao, Zerong Zheng, Hanzhang Tu, Boning Liu, Hongwen Zhang, and Yebin Liu. 2023. Tensor4d: Efficient neural 4d decomposition for high-fidelity dynamic reconstruction and rendering. In *Proceedings of the IEEE/CVF Conference on Computer Vision and Pattern Recognition*. 16632–16642.
- [50] Xuelun Shen, Zhipeng Cai, Wei Yin, Matthias Müller, Zijun Li, Kaixuan Wang, Xiaozhi Chen, and Cheng Wang. 2024. GIM: Learning Generalizable Image Matcher From Internet Videos. *arXiv preprint arXiv:2402.11095* (2024).
- [51] Liangchen Song, Anpei Chen, Zhong Li, Zhang Chen, Lele Chen, Junsong Yuan, Yi Xu, and Andreas Geiger. 2023. Nerfplayer: A streamable dynamic scene representation with decomposed neural radiance fields. *IEEE Transactions on Visualization and Computer Graphics* 29, 5 (2023), 2732–2742.
- [52] Cheng Sun, Min Sun, and Hwann-Tzong Chen. 2022. Direct voxel grid optimization: Super-fast convergence for radiance fields reconstruction. In *Proceedings of the IEEE/CVF Conference on Computer Vision and Pattern Recognition*. 5459–5469.
- [53] Chaoyang Wang, Ben Eckart, Simon Lucey, and Orazio Gallo. 2021. Neural Trajectory Fields for Dynamic Novel View Synthesis. , arXiv:2105.05994 pages. <https://doi.org/10.48550/arXiv.2105.05994>
- [54] Chen Wang, Jiadai Sun, Lina Liu, Chenming Wu, Zhelun Shen, Dayan Wu, Yuchao Dai, and Liangjun Zhang. 2023. Digging into depth priors for outdoor neural radiance fields. In *Proceedings of the 31st ACM International Conference on Multimedia*. 1221–1230.
- [55] Chen Wang, Xian Wu, Yuan-Chen Guo, Song-Hai Zhang, Yu-Wing Tai, and Shi-Min Hu. 2022. Nerf-sr: High quality neural radiance fields using supersampling. In *Proceedings of the 30th ACM International Conference on Multimedia*. 6445–6454.
- [56] Feng Wang, Zilong Chen, Guokang Wang, Yafei Song, and Huaping Liu. 2024. Masked space-time hash encoding for efficient dynamic scene reconstruction. *Advances in Neural Information Processing Systems* 36 (2024).
- [57] Feng Wang, Sinan Tan, Xinghang Li, Zeyue Tian, Yafei Song, and Huaping Liu. 2023. Mixed neural voxels for fast multi-view video synthesis. In *Proceedings of the IEEE/CVF International Conference on Computer Vision*. 19706–19716.
- [58] Liao Wang, Qiang Hu, Qihan He, Ziyu Wang, Jingyi Yu, Tinne Tuytelaars, Lan Xu, and Minye Wu. 2023. Neural Residual Radiance Fields for Streamably Free-Viewpoint Videos. In *Proceedings of the IEEE/CVF Conference on Computer Vision and Pattern Recognition*. 76–87.
- [59] Peng Wang, Lingjie Liu, Yuan Liu, Christian Theobalt, Taku Komura, and Wenping Wang. 2021. Neus: Learning neural implicit surfaces by volume rendering for multi-view reconstruction. *arXiv preprint arXiv:2106.10689* (2021).
- [60] Chung-Yi Weng, Brian Curless, Pratul P Srinivasan, Jonathan T Barron, and Ira Kemelmacher-Shlizerman. 2022. Humannerf: Free-viewpoint rendering of moving people from monocular video. In *Proceedings of the IEEE/CVF conference on computer vision and pattern recognition*. 16210–16220.
- [61] Guanjun Wu, Taoran Yi, Jiemin Fang, Lingxi Xie, Xiaopeng Zhang, Wei Wei, Wenyu Liu, Qi Tian, and Xinggang Wang. 2023. 4d gaussian splatting for real-time dynamic scene rendering. *arXiv preprint arXiv:2310.08528* (2023).
- [62] Kaiqiang Xiong, Rui Peng, Zhe Zhang, Tianxing Feng, Jianbo Jiao, Feng Gao, and Ronggang Wang. 2023. CI-MVSNet: Unsupervised multi-view stereo with dual-level contrastive learning. In *Proceedings of the IEEE/CVF International Conference on Computer Vision*. 3769–3780.
- [63] Wangze Xu, Qi Wang, Xinghao Pan, and Ronggang Wang. 2024. HDPNERF: Hybrid Depth Priors for Neural Radiance Fields from Sparse Input Views. In *ICASSP 2024-2024 IEEE International Conference on Acoustics, Speech and Signal Processing (ICASSP)*. IEEE, 3695–3699.
- [64] Ziyi Yang, Xinyu Gao, Wen Zhou, Shaohui Jiao, Yuqing Zhang, and Xiaogang Jin. 2023. Deformable 3D Gaussians for High-Fidelity Monocular Dynamic Scene Reconstruction. , arXiv:2309.13101 pages. <https://doi.org/10.48550/arXiv.2309.13101>
- [65] Zeyu Yang, Hongye Yang, Zijie Pan, Xiatao Zhu, and Li Zhang. 2023. Real-time Photorealistic Dynamic Scene Representation and Rendering with 4D Gaussian Splatting. , arXiv:2310.10642 pages. <https://doi.org/10.48550/arXiv.2310.10642> Technical Report.
- [66] Yao Yao, Zixin Luo, Shiwei Li, Tian Fang, and Long Quan. 2018. Mvsnet: Depth inference for unstructured multi-view stereo. In *Proceedings of the European conference on computer vision (ECCV)*. 767–783.
- [67] Yao Yao, Zixin Luo, Shiwei Li, Tianwei Shen, Tian Fang, and Long Quan. 2019. Recurrent mvsnet for high-resolution multi-view stereo depth inference. In *Proceedings of the IEEE/CVF conference on computer vision and pattern recognition*. 5525–5534.
- [68] Yuyang Yin, Dejie Xu, Zhangyang Wang, Yao Zhao, and Yunchao Wei. 2023. 4dgen: Grounded 4d content generation with spatial-temporal consistency. *arXiv preprint arXiv:2312.17225* (2023).
- [69] Alex Yu, Ruilong Li, Matthew Tancik, Hao Li, Ren Ng, and Angjoo Kanazawa. 2021. Plenotrees for real-time rendering of neural radiance fields. In *Proceedings of the IEEE/CVF International Conference on Computer Vision*. 5752–5761.
- [70] Zehao Yu, Anpei Chen, Binbin Huang, Torsten Sattler, and Andreas Geiger. 2023. Mip-splatting: Alias-free 3d gaussian splatting. *arXiv preprint arXiv:2311.16493* (2023).
- [71] Zhengming Yu, Wei Cheng, Xian Liu, Wayne Wu, and Kwan-Yee Lin. 2023. MonoHuman: Animatable Human Neural Field from Monocular Video. In *Proceedings of the IEEE/CVF Conference on Computer Vision and Pattern Recognition*. 16943–16953.
- [72] Junyi Zheng, Chong Bao, Rui Chen, Zilong Dong, Guofeng Zhang, Hujun Bao, and Zhaopeng Cui. 2023. Mirror-NeRF: Learning Neural Radiance Fields for Mirrors with Whitted-Style Ray Tracing. , 4606–4615 pages. <https://doi.org/10.1145/3581783.3611857>
- [73] Jian Zhang, Jinchi Huang, Bowen Cai, Huan Fu, Mingming Gong, Chaohui Wang, Jiaming Wang, Hongchen Luo, Rongfei Jia, and Binqiang Zhao. 2022. Digging into radiance grid for real-time view synthesis with detail preservation. In *European Conference on Computer Vision*. Springer, 724–740.
- [74] Kai Zhang, Gernot Riegler, Noah Snively, and Vladlen Koltun. 2020. Nerf++: Analyzing and improving neural radiance fields. *arXiv preprint arXiv:2010.07492* (2020).
- [75] Zhe Zhang, Huachen Gao, Yuxi Hu, and Ronggang Wang. 2023. N2mvsnet: Non-local neighbors aware multi-view stereo network. In *ICASSP 2023-2023 IEEE International Conference on Acoustics, Speech and Signal Processing (ICASSP)*. IEEE, 1–5.
- [76] Zhe Zhang, Yuxi Hu, Huachen Gao, and Ronggang Wang. 2023. Bi-ClueMVSNet: Learning Bidirectional Occlusion Clues for Multi-View Stereo. In *2023 International Joint Conference on Neural Networks (IJCNN)*. IEEE, 1–8.
- [77] Zhe Zhang, Rui Peng, Yuxi Hu, and Ronggang Wang. 2023. Geomvsnet: Learning multi-view stereo with geometry perception. In *Proceedings of the IEEE/CVF Conference on Computer Vision and Pattern Recognition*. 21508–21518.
- [78] Shunyuhan Zheng, Boyao Zhou, Ruizhi Shao, Boning Liu, Shengping Zhang, Liqiang Nie, and Yebin Liu. 2023. Gps-gaussian: Generalizable pixel-wise 3d gaussian splatting for real-time human novel view synthesis. *arXiv preprint arXiv:2312.02155* (2023).
- [79] Xiaoyun Zheng, Liwei Liao, Jianbo Jiao, Feng Gao, and Ronggang Wang. 2024. Surface-sos: Self-supervised object segmentation via neural surface representation. *IEEE Transactions on Image Processing* (2024).
- [80] Xiaoyun Zheng, Liwei Liao, Xufeng Li, Jianbo Jiao, Rongjie Wang, Feng Gao, Shiqi Wang, and Ronggang Wang. 2024. PKU-DyMVHumans: A Multi-View Video Benchmark for High-Fidelity Dynamic Human Modeling. In *Proceedings of the IEEE/CVF Conference on Computer Vision and Pattern Recognition*. 22530–22540.

- [81] Zehao Zhu, Zhiwen Fan, Yifan Jiang, and Zhangyang Wang. 2023. FSGS: Real-Time Few-shot View Synthesis using Gaussian Splatting. *arXiv preprint arXiv:2312.00451* (2023).

A Overview

With in the supplementantary, we provide:

- Details of Adaptive Optimization in Sec. B
- Hyperparameter Settings in Sec. C
- More Results in Sec. D

B Details of Adaptive Optimization

Based on the unique temporal characteristics of each Gaussian primitive, we apply distinct optimization schedules. Integrating the state function over time intervals enables us to represent the sampling probability of Gaussian primitives in the temporal domain: $I = F(t_{end}) - F(t_{start})$. Here, $F(t)$ represents the cumulative distribution function (CDF) of the Gaussian primitive's state function $\gamma(t)$.

$$F(t) = P(x < t) = \int_{-\infty}^t e^{-k \frac{x-\tau}{\sigma}} dx, \quad (26)$$

We approximate $F(t)$ based on[35]:

$$Q(t) = \int_{-\infty}^t \frac{1}{\sqrt{2\pi}} e^{-\frac{x^2}{2}} dx = 1 - \frac{1}{e^{1+\alpha_1 t^3 + \alpha_2 t}}, \quad (27)$$

To transform it into the form of $F(t)$, we employ the method of integration by substitution:

$$x = \sqrt{2k} \frac{m - \tau}{\sigma} \quad (28)$$

$$Q(t) = \int_{-\infty}^{\frac{\sigma t}{\sqrt{2k}} + \tau} \frac{1}{\sqrt{2\pi}} e^{-\frac{(\sqrt{2k} \frac{m-\tau}{\sigma})^2}{2}} d(\sqrt{2k} \frac{m - \tau}{\sigma}) \quad (29)$$

$$= \int_{-\infty}^{\frac{\sigma t}{\sqrt{2k}} + \tau} \frac{1}{\sqrt{2\pi}} e^{-k \frac{m-\tau}{\sigma}} d(\sqrt{2k} \frac{m - \tau}{\sigma}) \quad (30)$$

$$= \int_{-\infty}^{\frac{\sigma t}{\sqrt{2k}} + \tau} \frac{1}{\sqrt{2\pi}} e^{-k \frac{m-\tau}{\sigma}} d(\sqrt{2k} \frac{m - \tau}{\sigma}) \quad (31)$$

$$= \int_{-\infty}^{\frac{\sigma t}{\sqrt{2k}} + \tau} \frac{1}{\sqrt{2\pi}} \frac{\sqrt{2k}}{\sigma} e^{-k \frac{m-\tau}{\sigma}} dm \quad (32)$$

$$= \frac{\sqrt{k}}{\sqrt{\pi}\sigma} \int_{-\infty}^{\frac{\sigma t}{\sqrt{2k}} + \tau} e^{-k \frac{m-\tau}{\sigma}} dm \quad (33)$$

$$= \frac{\sqrt{k}}{\sqrt{\pi}\sigma} F\left(\frac{\sigma t}{\sqrt{2k}} + \tau\right), \quad (34)$$

Therefore, we can obtain $F(t)$:

$$F(t) = \frac{\sqrt{\pi}\sigma}{\sqrt{k}} Q\left(\sqrt{2k} \frac{(t - \tau)}{\sigma}\right). \quad (35)$$

For each Gaussian primitive \mathcal{G}_i^{AD} with distinct σ_i and τ_i , we can derive $F_i(t)$ based on Eq. 35. Then, we obtain I_i for each \mathcal{G}_i^{AD} , thus adopting different optimization schedules for each Gaussian primitive.

C HyperParameters settings

We predominantly adhere to the hyperparameter settings of 3DGS[22]. Specifically, the batch size in training is set to 4, and we initialize the learning rate of Scale-aware Residual Field parameters at $3.2e-3$, which decays to $3.2e-6$ by the end of training. Similarly, we initialize the learning rates of all tiny MLP decoders at $1.6e-4$, decaying to $1.6e-7$ by the end of training. Furthermore, we opt to abandon the strategy of filtering out larger Gaussians in worldspace. Our decision stems from the observation that this strategy results in incomplete backgrounds in our framework, thereby compromising our rendering quality.

Different datasets are collected under different settings, corresponding to different initialization methods. For the D-NeRF dataset[42], which involves monocular synthesized scene data, we uniformly and randomly initialize 10,000 Gaussian primitives distributed within a cube of $[-1.3, 1.3]^3$. Additionally, the temporal position of each Gaussian is uniformly initialized within the range of 0 to 1. We adopt a warm-up strategy with 1,000 iterations to train the scene as static, compensating for geometric information loss due to the absence of initialized point clouds. We trained these synthesized scenes using a black background. Additionally, we set the opacity reset interval to 2,000 iterations to accelerate training. The total training duration is set to 20,000 iterations.

For the multi-view real-world Plenoptic Video dataset[26], we utilize point clouds generated by COLMAP as our initialization point cloud. To achieve more accurate scene boundaries, in addition to using point clouds from the first frame, we incorporate sparse point clouds generated from subsequent frames after undergoing sparse filtering. The total number of initial points for each scene is around 40,000. The temporal position of each Gaussian is also uniformly initialized within the range of 0 to 1. In this setting, warm-up is not necessary. We set the opacity reset interval to 3,000 iterations to align with 3DGS[22].

D More Results

Comparing with state-of-the-art (SOTA) methods[7, 12, 13, 15, 42, 61], the per-scene evaluation results are presented in Tab. D1 for the D-NeRF dataset. Similarly, for the Plenoptic Video dataset, the per-scene evaluation results compared with SOTA methods[2, 7, 13, 27, 31, 51, 57, 61, 65] are shown in Tab. D2.

In comparison with [61], more qualitative comparisons are presented in Fig. D1. More results regarding dynamic-static segmentation in real-world scenes are presented in Fig. D2. Additionally, the depth map can also be obtained through Gaussian splatting during the rendering process, as shown in Fig. D2.

Table D1: The per-scene evaluation results on the D-NeRF dataset. † denotes a dynamic Gaussian method.

Method	Bouncing Balls			Hellwarrior			Hook			Jumpingjacks		
	PSNR(dB)↑	SSIM↑	LPIPS↓	PSNR(dB)↑	SSIM↑	LPIPS↓	PSNR(dB)↑	SSIM↑	LPIPS↓	PSNR(dB)↑	SSIM↑	LPIPS↓
D-NeRF[42]	38.93	0.98	0.10	25.02	0.95	0.06	29.25	0.96	0.11	32.80	0.98	0.03
KPlanes-hybrid[13]	40.33	0.99	-	24.81	0.95	-	28.13	0.95	-	31.64	0.97	-
TiNeuVox-B[12]	40.73	0.99	0.04	28.17	0.97	0.07	31.45	0.97	0.05	34.23	0.98	0.03
V4D[15]	42.67	0.99	0.02	27.03	0.96	0.05	31.04	0.97	0.03	35.36	0.99	0.02
HexPlane[7]	39.69	0.99	0.03	24.24	0.94	0.07	28.71	0.96	0.05	31.65	0.97	0.04
4DGS[61]†	40.62	0.99	0.02	28.71	0.97	0.04	32.73	0.98	0.03	35.42	0.99	0.01
Ours	36.02	0.99	0.01	38.01	0.97	0.02	36.81	0.99	0.01	34.56	0.98	0.016
Method	Lego			Mutant			Standup			Trex		
	PSNR(dB)↑	SSIM↑	LPIPS↓	PSNR(dB)↑	SSIM↑	LPIPS↓	PSNR(dB)↑	SSIM↑	LPIPS↓	PSNR(dB)↑	SSIM↑	LPIPS↓
D-NeRF[42]	21.64	0.83	0.16	31.29	0.97	0.02	32.79	0.98	0.02	31.75	0.97	0.03
KPlanes-hybrid[13]	25.27	0.94	-	32.59	0.97	-	33.17	0.98	-	30.75	0.97	-
TiNeuVox-B[12]	25.02	0.92	0.07	33.61	0.98	0.03	35.43	0.99	0.02	32.70	0.98	0.03
V4D[15]	25.62	0.95	0.04	36.27	0.99	0.01	37.20	0.99	0.01	34.53	0.99	0.02
HexPlane[7]	25.22	0.94	0.04	33.79	0.98	0.03	34.36	0.98	0.02	30.67	0.98	0.03
4DGS[61]†	25.03	0.94	0.04	37.59	0.99	0.02	38.11	0.99	0.01	34.23	0.99	0.01
Ours	25.46	0.94	0.04	42.11	0.99	0.01	44.45	0.99	0.01	31.62	0.98	0.01

Table D2: The per-scene evaluation results on the Plenoptic Video dataset. † denotes a dynamic Gaussian method.

Method	Coffee Martini			Cook Spinach			Cut Beef		
	PSNR(dB)↑	DSSIM↓	LPIPS↓	PSNR(dB)↑	DSSIM↓	LPIPS↓	PSNR(dB)↑	DSSIM↓	LPIPS↓
KPlanes-hybrid[13]	29.99	0.024	-	32.60	0.017	-	31.82	0.017	-
Mix-Voxels-L[57]	29.63	0.024	0.106	32.25	0.016	0.099	32.40	0.016	0.088
NeRFPlayer[51]	31.53	-	0.085	30.56	-	0.113	29.35	-	0.144
HyperReel[2]	28.37	-	0.127	32.30	-	0.089	32.92	-	0.084
HexPlane[7]	-	-	-	32.04	0.015	0.082	32.55	0.013	0.080
Dynamic 3DGS[31]†	26.49	0.033	0.139	32.97	0.013	0.087	30.72	0.016	0.090
4DGS-Realtime[65]†	28.33	-	-	32.93	-	-	33.85	-	-
Spacetime-Gs[27]†	28.61	0.025	0.069	33.18	0.011	0.037	33.52	0.011	0.036
4DGS[61]†	27.34	0.048	-	32.46	0.026	-	32.90	0.022	-
Ours	28.96	0.021	0.061	33.19	0.012	0.038	33.91	0.021	0.038
Method	Flame Salmon			Flame Steak			Sear Steak		
	PSNR(dB)↑	DSSIM↓	LPIPS↓	PSNR(dB)↑	DSSIM↓	LPIPS↓	PSNR(dB)↑	DSSIM↓	LPIPS↓
KPlanes-hybrid[13]	30.44	0.024	-	32.38	0.015	-	32.52	0.013	-
Mix-Voxels-L[57]	29.81	0.026	0.116	31.83	0.014	0.088	32.10	0.012	0.080
NeRFPlayer[51]	31.65	-	0.098	31.93	-	0.088	29.13	-	0.138
HyperReel[2]	25.02	-	0.136	33.61	-	0.078	35.43	-	0.077
HexPlane[7]	29.47	0.018	0.078	31.82	0.012	0.071	32.23	0.012	0.070
Dynamic 3DGS[31]†	26.92	0.030	0.122	33.24	0.011	0.079	33.68	0.011	0.079
4DGS-Realtime[65]†	29.38	-	-	34.03	-	-	33.51	-	-
Spacetime-Gs[27]†	29.48	0.022	0.063	33.64	0.009	0.029	33.89	0.009	0.030
4DGS[61]†	29.20	0.042	-	32.51	0.023	-	32.49	0.022	-
Ours	29.14	0.021	0.059	33.83	0.010	0.034	33.89	0.010	0.036

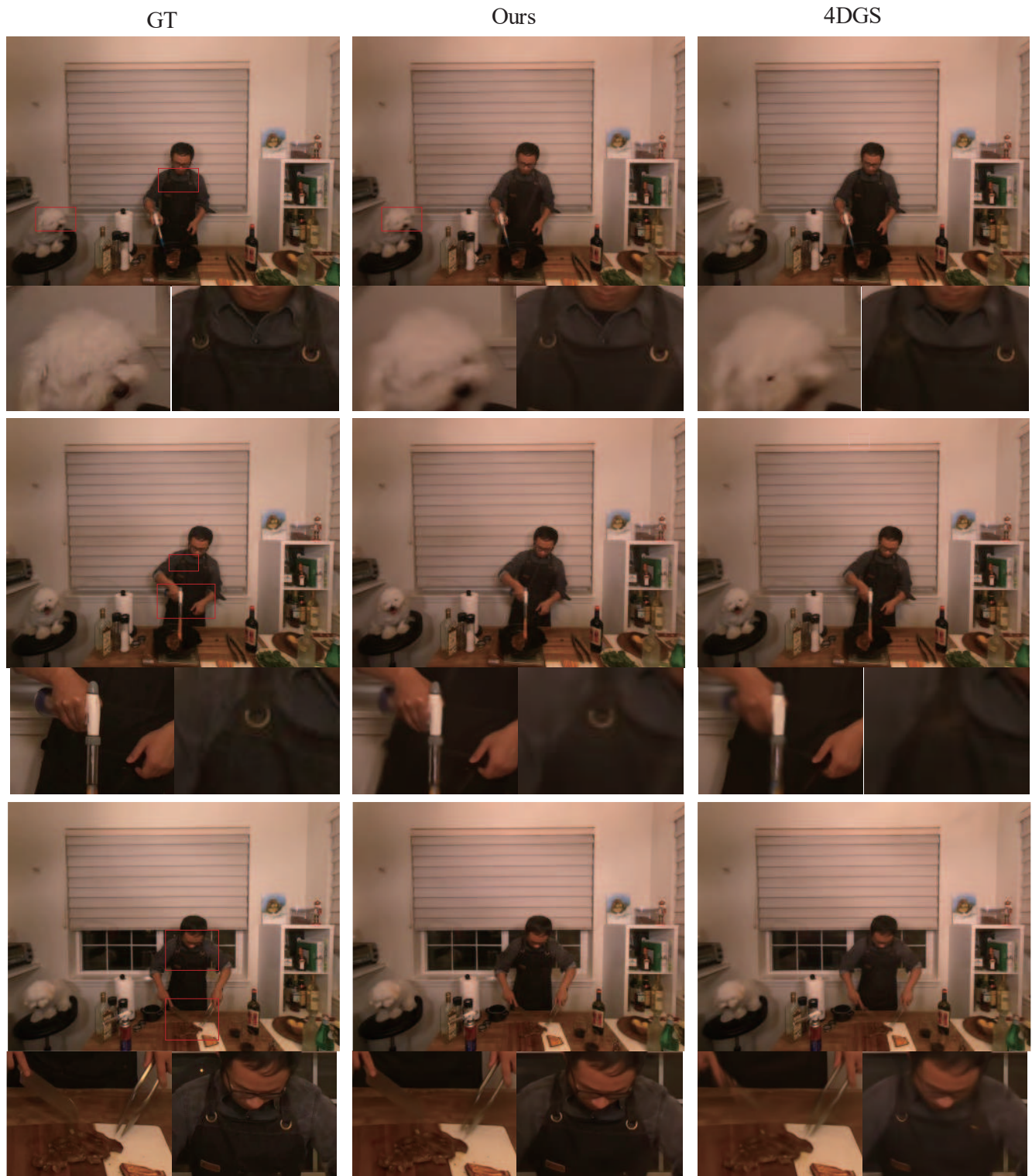


Figure D1: Qualitative comparison with [61] on the Plenoptic Video dataset.

Our rendering

Our depth map

Our segmentation

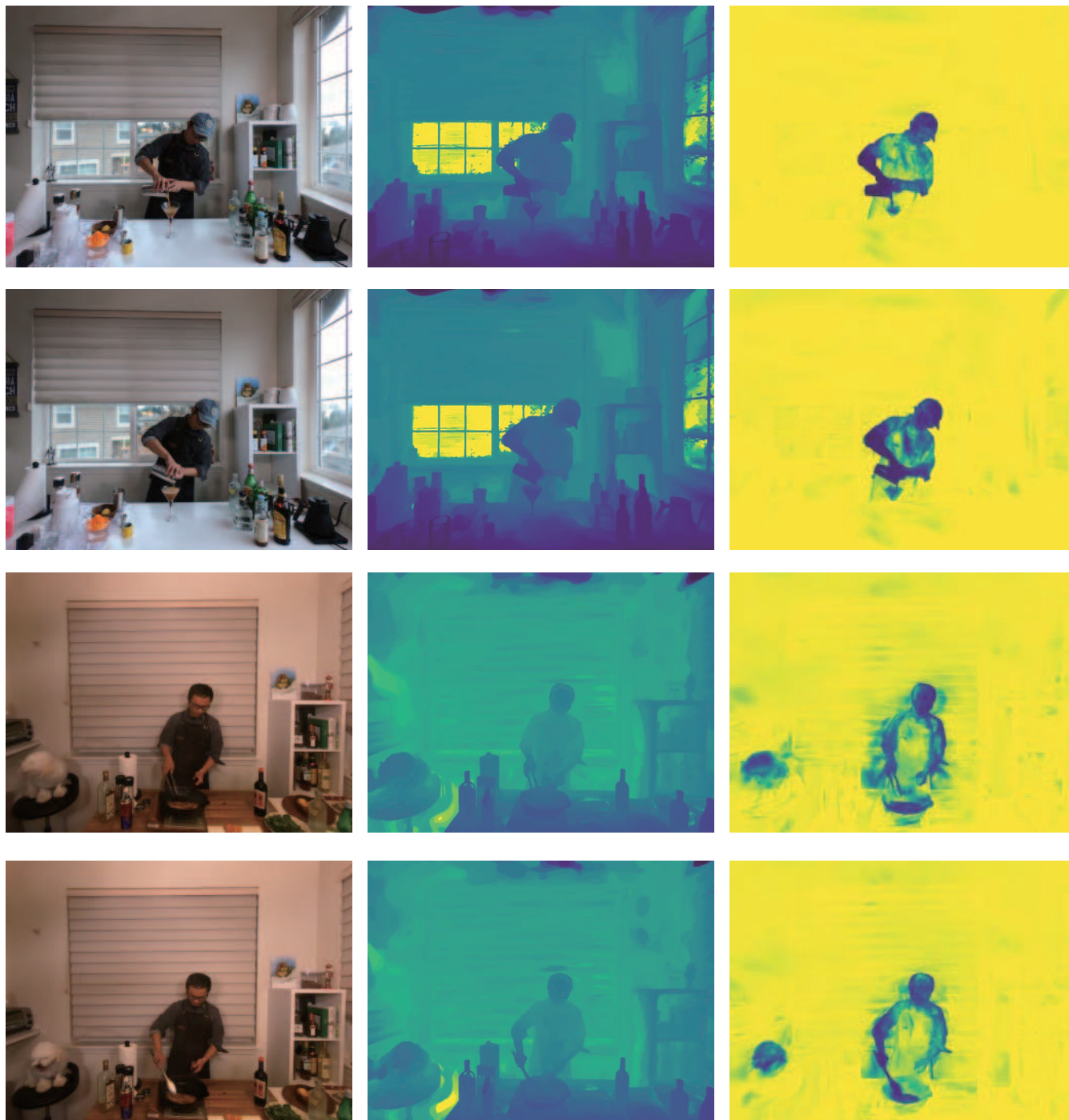


Figure D2: Depth map and Segmentation of dynamic and static scenes.